A coupled lattice Boltzmann/finite volume method for turbulent gas-liquid bubbly flows

Daniel Lauwers[*], **Matthias Meinke**[*,†] **and Wolfgang Schröder**[*,†]

[*] Chair of Fluid Mechanics and Institute of Aerodynamics
RWTH Aachen University
Wüllnerstr. 5a, 52062 Aachen, Germany
e-mail: {d.lauwers, m.meinke, office}@aia.rwth-aachen.de

[†] JARA Center for Simulation and Data Science
RWTH Aachen University
Seffenter Weg 23, 52074 Aachen, Germany

Key words: Eulerian-Eulerian model, bubbly flow, lattice Boltzmann, finite volume, LES

Abstract: *A simulation method for large eddy simulations (LES) of dispersed gas-liquid bubbly flows based on an Eulerian-Eulerian (E-E) model is presented. A volume averaging approach is used resulting in a set of conservation equations for each phase. The liquid phase is predicted using a lattice Boltzmann method, while the gas phase is modeled by a finite volume method. Interface terms between the phases result in a two-way coupled system. Both methods are formulated on a shared Cartesian grid similar to the concept in [1], which facilitates the exchange of coupling terms between the two solvers and an efficient implementation on high-performance computing (HPC) hardware. This coupled multiphase approach combines the advantages of the lattice Boltzmann (LB) method as an efficient prediction tool for low Mach number flows with those of a finite volume method used for the modeling of the phase with larger density changes by solving the Navier-Stokes equations. To accurately model the turbulent motion of the liquid phase on all resolved scales, a cumulant-based collision step for the lattice Boltzmann method [2] is combined with a Smagorinsky sub-grid-scale turbulence model. In the finite volume solver, the effect of the sub-grid-scale turbulence is incorporated according to the MILES approach. For the validation of the new method, large-eddy simulations of turbulent bubbly flows are performed. The accuracy of the predictions is evaluated comparing the results to experimental reference data for a generic test case, for which good agreement is found. The applicability of the method will be demonstrated for a bubbly turbulent channel flow, which mimics the phenomena in the electrochemical machining (ECM) process.*

1 INTRODUCTION

The study of gas-liquid multiphase flows has been an active research topic for many decades. They occur in processes belonging to industries including chemical, pharmaceutical, food, energy, and machinery industries. The quest for an improved design of these processes, generates an increasing demand for the accurate prediction and detailed analysis of such two-phase flows. Multiphase gas-liquid flows can be classified in many categories, mainly depending on the gas-liquid volume ratio and the bubble size. Here, we consider a dispersed phase in a carrier phase, such as small gas bubbles in liquids or liquid droplets in a gas.

The technical application for which the current method is developed, is an electrochemical machining (ECM) process, in which gas bubbles are generated in a liquid electrolyte during the electrochemical removal of material. Since the local removal rate of material depends on the electrical current and the gas is non-conductive, the local gas concentration greatly influences the process speed and the geometry of the final workpiece. Therefore, a detailed prediction of the highly unsteady gas transport phenomena in the electrolyte flow is important for a good design of the ECM process. The simulation results can be used to identify process parameters

https://doi.org/10.4995/YIC2021.2021.12211

and a tool geometry for an improved accuracy of the workpiece geometry without deviations caused by, e.g., local gas agglomerations.

The turbulence modeling in E-E models of gas-liquid bubbly flows can be based on the Reynolds-averaged Navier-Stokes (RANS) or large eddy simulation (LES) approaches. In the LES, the larger turbulent scales are fully resolved, whereas in RANS methods all turbulent motions are filtered from the flow field and modeled by additional transport equations. This leads to less strict spatial resolution requirements compared to LES but limits the level of details that can be predicted. In LES, the turbulent motion is explicitly resolved up to a certain spatial filter width, which is usually on the order of the local spatial step. LES typically provides more accurate results where the assumptions of the RANS models do not hold, i.e., typically in flows with strong streamline curvature, adverse pressure gradients or in large scale vertical motion in separated flow regions or wakes. Since such flows might occur in the ECM process, an LES method should be used.

In the following, a brief overview over existing E-E modeling approaches for gas-liquid bubbly flow is given. Early examples of LES methods for E-E models are the works of Milelli et al. [3] and Deen et al. [4]. In both cases, the E-E model is implemented by extending the commercial ANSYS CFX code, that is based on the finite volume (FV) method. Many authors improved on these works by studying certain aspects of the earlier models in more detail [5]. In particular, the interface forces between the phases and the sub-grid scale modeling of turbulence in the liquid phase are discussed. Recent studies include [6], [7], and [8], in which different solver types based on a finite volume formulation are used for the two sets of conservation equations. While the finite volume method is capable of producing excellent results, it is computationally more expensive compared to the lattice Boltzmann (LB) method. The LB method has been successfully used for direct numerical simulations (DNS) of gas-liquid flows [9]. DNS, however, becomes too expensive for dispersed bubbles in high Reynolds number flow. Sungkorn et al. [10] performed LES of bubble columns using the Eulerian-Lagrangian (E-L) approach with the LB method. Recently, an E-E model solved with coupled FV and LB solvers was presented by Shu et al. [11], which was, however, based on the RANS approach and which used a coupling strategy of the solvers different from that presented in this study.

This paper is organized as follows. The details of the method will be described in Sections 2 and 3. Validation results for the method are shown in Section 4. Finally, the application to an ECM setup is shown in Section 5, where results of the LES of turbulent gas-liquid channel flows, similar to the electrolyte flow in the ECM process are presented.

2 PHYSICAL MODELING

The phase averaged Eulerian-Eulerian conservation equations for mass and momentum are given by [12, 5]

$$\frac{\partial \alpha_k \bar{\bar{\rho}}_k}{\partial t} + \nabla \cdot (\alpha_k \bar{\bar{\rho}}_k \hat{\boldsymbol{v}}_k) = \Gamma_k \tag{1}$$

$$\frac{\partial \alpha_k \bar{\bar{\rho}}_k \hat{\boldsymbol{v}}_k}{\partial t} + \nabla \cdot (\alpha_k \bar{\bar{\rho}}_k \hat{\boldsymbol{v}}_k \hat{\boldsymbol{v}}_k) = -\alpha_k \nabla \hat{p} - \nabla \cdot (\alpha_k \hat{\boldsymbol{\tau}}_k) + \alpha_k \bar{\bar{\rho}}_k \boldsymbol{g} + \boldsymbol{M}_k \ . \tag{2}$$

The quantity k represents the gas or liquid component of the fluid, i.e., g for gas and l for liquid, and α_k is the local void fraction of the phase, which represents the probability of finding the corresponding phase at a certain location in time and space. For the gas-liquid flow, the condition $\alpha_g + \alpha_l = 1$ holds. The other variables are the density ρ, velocity v, pressure p, viscous fluxes $\boldsymbol{\tau}$, and the gravity vector $\boldsymbol{g}$. The mass and momentum transfer terms between the two phases are denoted Γ and $\boldsymbol{M}$. The symbols $\bar{\bar{\cdot}}$ and $\hat{\cdot}$ define the phase averaging and mass weighted averaging operators [12].

2.1 Model simplifications

The Eulerian-Eulerian model equations Eq. (1) and (2) can become stiff and difficult to solve due to possibly large two-way coupling terms resulting from the interfacial force terms, which are discussed in Section 2.2, and the influences of the coupled void fractions α_k. Some models avoid these difficulties by completely neglecting the influence of the dispersed phase on the liquid phase. These one-way coupled models are valid only for cases, where the motion of the liquid phase is dominated by external forces and the volume fraction of the gas phase is very low. A more accurate approach can be derived for the liquid phase via the mixture balance equations [13, 12]. Exploiting the fact that the density difference between gas and liquid is large, the influence of the void fraction α_k can be removed from all terms of the liquid momentum equation for moderate void fractions except for the gravity term. This simplification is similar to the Boussinesq approximation for the single-phase momentum balance equations. In that case, changes in density due to temperature changes are also neglected in all terms except for the gravity term. Additionally, no mass transfer between the phases is present in our case, hence $\Gamma_g = \Gamma_l = 0$. This leads to the following conservation equations for the liquid phase

$$\frac{\partial \bar{\bar{\rho}}_l}{\partial t} + \nabla \cdot (\bar{\bar{\rho}}_l \hat{\boldsymbol{v}}_l) = 0 \tag{3}$$

$$\frac{\partial \bar{\bar{\rho}}_l \hat{\boldsymbol{v}}_l}{\partial t} + \nabla \cdot (\bar{\bar{\rho}}_l \hat{\boldsymbol{v}}_l \hat{\boldsymbol{v}}_l) = -\nabla \hat{p} - \nabla \cdot \hat{\boldsymbol{\tau}}_l + \alpha_l \bar{\bar{\rho}}_l \boldsymbol{g} \ . \tag{4}$$

These equations only differ from their single-phase counterparts by the last term of the momentum equation. This makes it possible to use a standard solution procedure for a single phase with only minor changes for the solution of the liquid phase flow.
The balance equations for the gas phase resemble the base E-E equations Eq. (1) and (2) much more closely. Like in [13], an additional diffusive term is added to the mass equation of the gas phase to model the bubble path dispersion. This diffusion effect is caused by the interaction of bubbles with the turbulent wake of other bubbles. This effect causes a diverging flow pattern of the ascending bubbles in locally aerated bubble columns. It can also be described using a drifting velocity $\boldsymbol{v}_{drift}$ that reads [13]

$$\boldsymbol{v}_{drift} = -\frac{1}{Sc} \frac{\mu_{l,turb}}{\bar{\bar{\rho}}_l} \boldsymbol{I} \cdot \frac{1}{\alpha_g} \nabla \alpha_g \ . \tag{5}$$

The Schmidt number Sc is usually assumed to be $Sc = 1$ for the bubble path dispersion. The quantity $\mu_{l,turb}$ is the turbulent viscosity of the liquid phase that is representative for the wake of the bubbles. The resulting conservation equations of the gas phase are

$$\frac{\partial \alpha_g \bar{\bar{\rho}}_g}{\partial t} + \nabla \cdot (\alpha_g \bar{\bar{\rho}}_g \hat{\boldsymbol{v}}_g) = \frac{1}{Sc} \nabla \cdot (\mu_{l,turb} \frac{\bar{\bar{\rho}}_g}{\bar{\bar{\rho}}_l} \nabla \alpha_g) \tag{6}$$

$$\frac{\partial \alpha_g \bar{\bar{\rho}}_g \hat{\boldsymbol{v}}_g}{\partial t} + \nabla \cdot (\alpha_g \bar{\bar{\rho}}_g \hat{\boldsymbol{v}}_g \hat{\boldsymbol{v}}_g) = -\alpha_g \nabla \hat{p} - \nabla \cdot (\alpha_g \hat{\boldsymbol{\tau}}_g) + \alpha_g \bar{\bar{\rho}}_g \boldsymbol{g} + \boldsymbol{M}_g \ . \tag{7}$$

2.2 Interfacial forces

The interfacial forces represent the forces that the individual bubbles experience during the movement through the liquid phase. The relevant forces are the drag force $\boldsymbol{F}_D$, the lift force $\boldsymbol{F}_L$, the virtual mass force $\boldsymbol{F}_{VM}$, and the turbulent dispersion force $\boldsymbol{F}_{TD}$ [8]

$$\boldsymbol{M}_g = \boldsymbol{F}_D + \boldsymbol{F}_L + \boldsymbol{F}_{VM} + \boldsymbol{F}_{TD} \ . \tag{8}$$

The corresponding reaction forces on the liquid phase are disregarded in the liquid momentum equation Eq. (4), due to the large difference in density between the phases. For the closure of the force terms, the equations described in [8] are used.
The drag force is modeled as

$$\boldsymbol{F}_D = \frac{3}{4}\alpha_g C_D \frac{\bar{\bar{\rho}}_l}{d_B}|\hat{\boldsymbol{v}}_l - \hat{\boldsymbol{v}}_g|(\hat{\boldsymbol{v}}_l - \hat{\boldsymbol{v}}_g) \tag{9}$$

with the bubble diameter d_B and the coefficient of drag C_D. For the distorted bubble regime, the drag coefficient C_D can be estimated [12]

$$C_D = \frac{2}{3}\sqrt{Eo} \tag{10}$$

with the Eötvös number $Eo = |\boldsymbol{g}|(\rho_l - \rho_g)d_B^2/\sigma$. The quantity σ represents the surface tension of the liquid phase. The distorted bubble regime is applicable for the bubble column in Section 4. For the simulation in Section 5, Stokes' drag law is assumed since the bubbles are sufficiently small to be considered spherical [12]

$$C_D = \frac{24}{Re_B} = \frac{24\ \nu_l}{|\hat{\boldsymbol{v}}_l - \hat{\boldsymbol{v}}_g|\ d_B}\ . \tag{11}$$

The lift force is modeled by

$$\boldsymbol{F}_L = C_L \alpha_g \bar{\bar{\rho}}_l (\hat{\boldsymbol{v}}_g - \hat{\boldsymbol{v}}_l) \times (\nabla \times \hat{\boldsymbol{v}}_l)\ . \tag{12}$$

The correct coefficient of lift C_L for bubbly flows has been a controversial topic. In the review paper [5], the values range from -0.05 to 0.5. In principle, the value and sign of the lift force highly depends on the shape of the bubble and the flow conditions around it. A widely adopted variable model for the coefficient of lift is the Tomiyama lift force model [14]. This leads to $C_L = 0.288$ for the validation case studied in this work, when the Morton number is extrapolated for an air-water mixture. Tomiyama's model, however, was obtained for single bubbles under static shear flow conditions, that differ from turbulent dispersed bubbly flows. In recent studies, Shu et al. [11] have shown that simulations of buoyancy driven bubbly flows can be performed without lift force. Because of the uncertainties regarding the value of the lift coefficient for the different flow regimes studied in this work, the lift force is taken here as zero.
The virtual mass force is modeled by

$$\boldsymbol{F}_{VM} = C_{VM}\alpha_g \bar{\bar{\rho}}_l \left[\left(\frac{\partial \hat{\boldsymbol{v}}_l}{\partial t} + (\hat{\boldsymbol{v}}_l \cdot \nabla)\hat{\boldsymbol{v}}_l\right) - \left(\frac{\partial \hat{\boldsymbol{v}}_g}{\partial t} + (\hat{\boldsymbol{v}}_g \cdot \nabla)\hat{\boldsymbol{v}}_g\right)\right] \tag{13}$$

with the virtual mass coefficient $C_{VM} = 0.5$.
The turbulent dispersion force is

$$\boldsymbol{F}_{TD} = -\frac{3}{4}\frac{C_D}{Sc}\frac{\mu_{l,eff}}{d_B}|\hat{\boldsymbol{v}}_l - \hat{\boldsymbol{v}}_g|\nabla\alpha_g \tag{14}$$

with the effective liquid viscosity $\mu_{l,eff}$ (see Section 2.3).

2.3 Turbulence modeling

Since in LES not all the scales of turbulent motion are resolved in the continuous phase, the influence of the sub-grid scale (SGS) motions have to be modeled. In this work, a Smagorinsky SGS model is chosen due to its previous successful application to bubble columns [5]. In addition

to the influence of the SGS turbulence, bubble induced turbulence (BIT) must be accounted for in the simulation of bubbly flows. Thus, the effective viscosity of the liquid phase is the sum of the molecular viscosity, the viscosity due to the SGS of turbulence and the BIT contribution

$$\mu_{l,eff} = \mu_{l,M} + \mu_{l,SGS} + \mu_{l,BIT} \ . \tag{15}$$

The equation for the SGS viscosity μ_{SGS} is

$$\mu_{l,SGS} = \bar{\bar{\rho}}_l (C_S \Delta)^2 \sqrt{2 \boldsymbol{S}_{ij} \boldsymbol{S}_{ij}} \tag{16}$$

as a function of the Smagorinsky constant C_S, the rate-of-strain tensor $\boldsymbol{S}_{ij}$, and the grid filter width Δ. In this study, $C_S = 0.1$ is used for all simulations.
For the BIT viscosity, the model from [3, 8] is used

$$\mu_{l,BIT} = C_S \Delta \bar{\bar{\rho}}_l \alpha_g |\hat{\boldsymbol{v}}_g - \hat{\boldsymbol{v}}_l| \ . \tag{17}$$

The influence of the turbulent motion in the gas phase is incorporated according to the MILES approach [15].

3 NUMERICAL METHOD

The Eulerian-Eulerian model described in Section 2 is implemented in the multiphysics solver mAIA – formerly denoted ZFS – developed by the Institute of Aerodynamics of RWTH Aachen University [16]. One of the strengths of mAIA is the coupling concept that allows multiple solvers of different type to share simulation data in a common data structure. In this study, a lattice Boltzmann (LB) solver representing the liquid phase is coupled to a finite volume (FV) solver for the gas phase. This approach combines the advantages of the LB method as an efficient prediction tool for low Mach number flows with those of the FV method for the phase with higher density changes. Both solvers are implemented for the efficient parallel execution on HPC hardware, which enables the simulation of problems requiring a large number of mesh cells as the simulations discussed in Sections 4 and 5. Both methods are discretized on hierarchical Cartesian meshes, which allows a straightforward local mesh refinement with dynamic load balancing. For the generic cases simulated in this paper, however, local grid refinement was not necessary.

3.1 Description of the solvers

The conservation equations for the liquid phase Eq. (3) and (4) are identical to their single-phase counterparts except for the buoyancy term. Therefore, only minor modifications to the single-phase LB solver are necessary. The LB method is based on the discrete Boltzmann equation with the Bhatnagar-Gross-Krook approximation [17]. The particle probability distribution functions (PDFs) are discretized in this study according to the D3Q27 model [18] in a cell-centered approach. A cumulant based collision step [2] is used that is capable of producing accurate results across a wide range of Reynolds numbers. This is important due to the highly turbulent nature of the studied gas liquid bubbly flows. In contrast to the multi-relaxation time (MRT) approach, the cumulant based collision step does not require the tuning of model parameters. The buoyancy term of the momentum equation Eq. (4) is implemented according to [19], adding the force components to the PDFs before the propagation step.

The finite volume method solving the gas conservation equations combines an advective upstream splitting method (AUSM) with the second-order accurate monotone upstream centered scheme for conservation laws (MUSCL) approach for the computation of the inviscid fluxes. The viscous fluxes are discretized by a second-order accurate centered scheme as well. Time

integration is accomplished by an explicit, low-storage 5-step Runge-Kutta method. The gas momentum equations become stiff due to the momentum exchange terms in Eq. (8). To maintain numerical stability, the explicit time-integration scheme is modified for the momentum equations. The influence of the drag, turbulent dispersion and the local term of the virtual mass forces are incorporated by an implicit Crank–Nicolson scheme, while the explicit formulation is kept for the remaining terms.

3.2 Solution procedure

The time steps of the two solvers are synchronized by using the constant time step of the LB solver also for the finite volume method. Due to the strongly two-way coupled nature of the conservation equations of the two phases, the flow solvers operate in a staggered approach in time direction. First, the liquid phase solver completes a time-step using the gas void fraction field of the previous time step. The resulting updated liquid velocity and pressure field is then transferred to the gas phase solver. Secondly, the gas solver completes its time step, consisting of the following procedure. The density distribution is updated with the liquid pressure field. The changes in gas velocity and gas void fraction are obtained by the solution of the gas mass and momentum equations in each Runge-Kutta step. Finally, the updated gas flow variables are transferred to the liquid flow solver for the next time step.

4 VALIDATION OF THE METHOD

For the validation of the numerical method, a standard test case for turbulent, buoyancy driven bubbly flow is simulated. It was first studied experimentally and numerically by Deen et al. [20, 4]. Air is injected at the bottom surface into a water column with a height H of $H = 0.45$ m and a square cross-section $W \times D$ of 0.15×0.15 m^2. The bubbles enter the duct geometry through a perforated plate with 49 holes at the center of the bottom surface. The holes have a diameter of 1 mm and are arranged in a square pattern of 7×7 holes with a pitch of 6.25 mm. At the top, the water forms a free surface through which the injected air escapes. The gas velocity above the water surface is specified as 4.9×10^{-3} m s^{-1}, which leads to a gas flow rate of 1.1×10^{-4} m^3 s^{-1} at ambient pressure. The diameter of the resulting bubbles d_B is 4.0 mm [4]. This test case has been extensively studied for the validation of numerical models for bubbly flows. Recent studies that feature simulation results of this setup are [6, 7, 8, 11].

For the present simulations, a uniform, unstructured Cartesian grid with $44 \times 44 \times 128$ cells is used to discretize the bubble column. For the liquid phase, no-slip boundary conditions are applied at the column walls and bottom surface. The interpolated bounce back following the BFL rule is used for these boundaries [21]. The water surface is modeled by a slip-wall boundary condition. The gas flow rate is enforced in the inflow boundary condition. Furthermore, a no-slip condition is applied to the walls and the remaining bottom surface. For the outflow, a pressure outflow boundary condition is imposed to the top surface. The time step of the simulation is constant at 6.77×10^{-4} s.

The bubble diameter d_B is assumed to be 4 mm, bubble coalescence or break-up are not accounted for in this study. The original experiment was designed to minimize coalescence of bubbles by adding salt to the water [20]. The change in bubble diameter due to the varying hydrostatic pressure is also neglected. This approximation is justified since the increase in bubble diameter over the height of the column only amounts to about 1.4 %.

4.1 Instantaneous results

The flow field of the bubble column is mainly determined by a bubble plume meandering in the column. The liquid flow field is turbulent and strongly influenced by the location of the

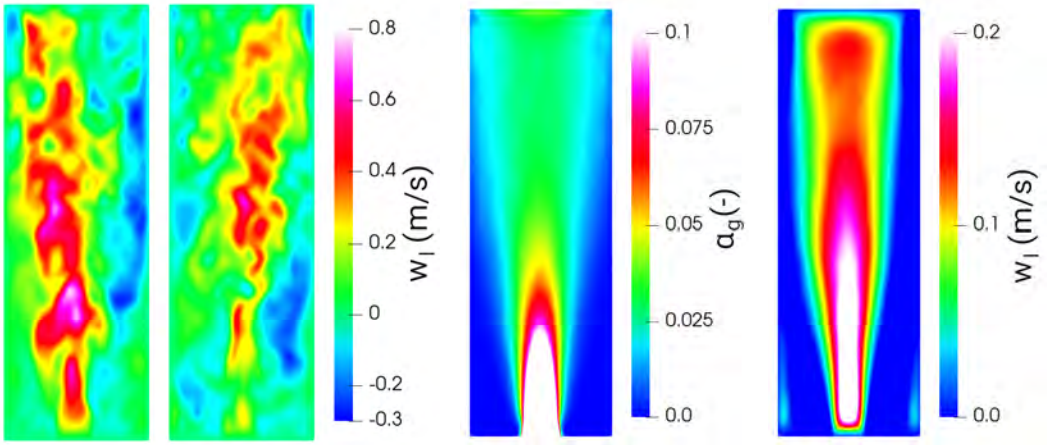

(a) (b) (c)

Figure 1: Liquid axial velocity at the times $t = 67.7$ s and $t = 135.3$ s (a), average gas void fraction (b) and average liquid axial velocity (c) at the mid-plane of the column.

bubble plume. Close to the plume, the liquid moves predominantly in the upward direction due to the buoyancy of the gas phase. The axial component of the liquid velocity at the mid-plane is shown in Figure 1(a) for two time levels, $t = 67.7$ s and $t = 135.3$ s.

4.2 Time-averaged results

For the generation of time-averaged results and turbulence statistics, 100,000 time steps are performed first, to obtain a fully developed flow field before the time averaging begins. The averaging is based on an additional 400,000 time steps. This corresponds to an averaging window from 68 s to 271 s in physical time.

In Figures 1(b) and 1(c), the averaged liquid axial velocity and gas void fraction in the mid-plane of the column are displayed. In the bottom part of the column, the gas void fraction is confined to a narrow, but diverging area. Due to the movement of the bubble plume, this differs from the top part of the column, where gas can be found over the full width of the column. The highest liquid velocity values are found in the region close to the gas inlet. Near the walls, a recirculation region with negative velocity values is visible. In the bottom corners, vortices are formed in the liquid phase.

In Figures 2(a) and 2(b), the liquid and gas axial velocities at the mid-plane are plotted along a line at the height of 25 cm above the bottom of the column. The liquid axial velocity agrees well with the experimental data of Deen [4]. The gas axial velocity is somewhat underestimated, especially in the center region of the column.

In Figures 2(c) and 2(d), the root-mean-square of the fluctuating liquid axial velocity w_l' and the turbulent kinetic energy $TKE_l = 0.5\ (u_l'u_l' + v_l'v_l' + w_l'w_l')$ are plotted. The turbulent fluctuations of the liquid phase flow are slightly overestimated by the present method except for the region near the walls, where the intensity must vanish. Both graphs exhibit a dent near the center of the column, that is visible in the simulation results and the experiments. The asymmetry of the results indicates that the time averaging interval is not sufficient, which can be attributed to the highly unsteady character of the test case featuring low frequency variations from the meandering bubble column. This may also explain a part of the visible deviations of the numerical solution.

5 SIMULATIONS OF A TURBULENT CHANNEL FLOW

The presented method is applied to a generic setup of the gas-liquid flow as it occurs in the ECM process in the gap between the tool and the work piece. This multiphase flow is studied

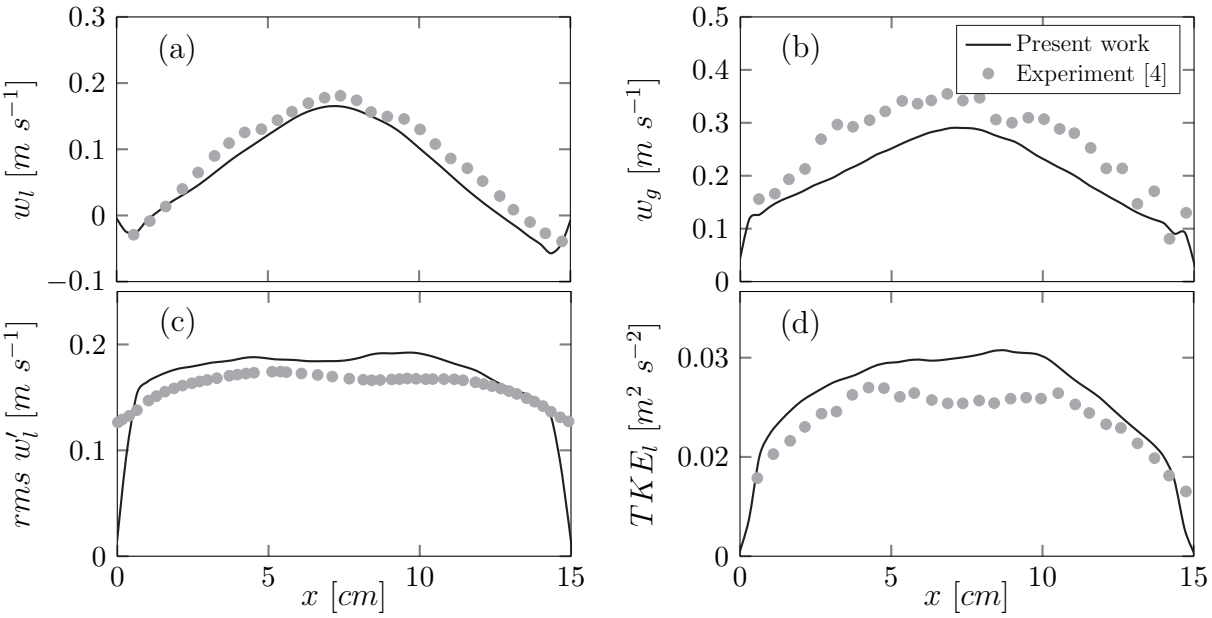

Figure 2: Averaged liquid (a) and gas (b) axial velocity, root-mean-square of the fluctuating liquid axial velocity (c) and liquid turbulent kinetic energy (d) at a height of $z = 25$ cm in comparison with measurements from [4].

experimentally and numerically in the research project described in [22]. For the experimental investigations, the flow is upscaled from a gap height of 1×10^{-4} m to a gap height of 1×10^{-2} m, keeping the Reynolds number constant. This upscaled machining gap is modeled as a turbulent channel flow with a Reynolds number of $Re = 3000$ based on the channel height and the mean flow velocity. The machining process is imitated by the introduction of gas bubbles through the bottom or top wall of the channel with a constant flow rate. As a starting condition, a fully developed turbulent channel flow is generated. The friction velocity based Reynolds number Re_τ of this single-phase flow is approximately $Re_\tau = 100$. To capture the large turbulent structures that are present in such a low Re_τ flow, a simulation domain of $1H \times 3H \times 12H$ channel heights is used in the wall normal, spanwise, and streamwise direction. The no-slip boundary condition is applied at the top and bottom boundary, and periodic conditions for the remaining boundaries. A volume force in the main flow direction is applied to keep a constant volume flow rate. The simulation domain is discretized with a uniform, Cartesian grid using $100 \times 300 \times 1200$ cells leading to a Δy^+ of 2.07. The gas flow rate per channel height unit is chosen to be 1/500 of the average liquid flow rate in the channel. The liquid is modeled as water with a density of 1000 kg m^{-3} and a kinematic viscosity of 1×10^{-6} m^2 s^{-1}. The gas is air with a density of 1.2 kg m^{-3} at atmospheric pressure and a kinematic viscosity of 1.52×10^{-5} m^2 s^{-1}. Gravity acts in the downward direction with the acceleration of 9.81 m s^{-2}. The bubble diameter is estimated to be 10^{-4} m, which is equal to the mesh cell size.

Figure 3 shows instantaneous gas void fraction fields for the gas injection from the bottom and the top of the channel. The effect of the buoyancy is clearly visible. In the case of the injection from the bottom wall, the gas is much more distributed throughout the channel. The large turbulent structures of the channel flow lead to areas of severely varying gas void fraction along the axis of the channel. In the case of the injection from the top of the channel, the buoyancy prevents the gas bubbles to be distributed throughout the channel. A nearly uniform layer of higher gas void fraction in formed at the top wall.
The averaged liquid velocity profiles in Figure 4 reflect this difference in the gas distribution. For the injection from the bottom wall, the velocity profile stays much more symmetric after the initial distribution of the bubbles. Compared to the single-phase profile, the velocity gradients

at the walls increase after the gas injection due to the increased momentum exchange normal to the walls. In the case of the injection from the top of the channel, the velocity profile becomes increasingly asymmetric. In this case, the buoyancy of the gas bubbles prevent momentum transfer in the top region of the channel enabling higher axial velocities in the top half of the channel.

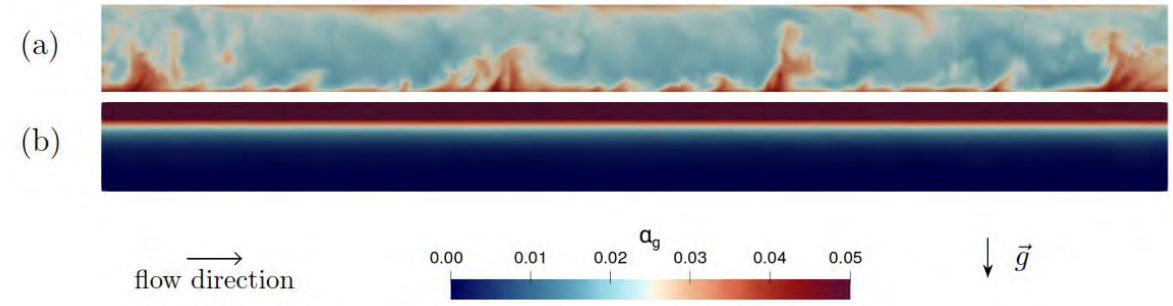

Figure 3: Instantaneous gas void fraction at t = 0.385 s after gas injection from the bottom (a) and the top (b) walls into the turbulent channel flow.

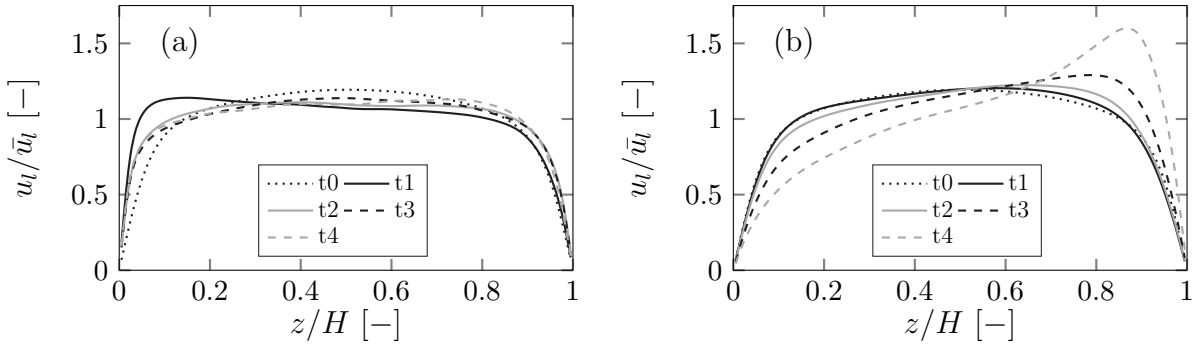

Figure 4: Averaged relative liquid velocity distribution plotted over the distance from the channel bottom wall for the times t1 = 0.192 s, t2 = 0.385 s, t3 = 0.577 s and t4 = 0.770 s after the start of the gas injection at time t0. Gas injection from the bottom wall (a) and the top wall (b).

6 CONCLUSION

A coupled lattice Boltzmann/finite volume method for the Eulerian-Eulerian simulation of gas-liquid bubbly flows is presented. The novel method is validated with LES of Deen's bubble column case. The model is capable of reproducing the meandering of the bubble plume in the column. The averaged results show good agreement with the experimental data. An engineering application of the method is shown with the simulation of a turbulent channel flow, similar to the gas-liquid electrolyte flow during the ECM process. The method predicts the expected large differences in the gas distribution depending on the location of the gas generation. Since the local gas void fraction has a strong influence on the geometry of the workpieces produced with the ECM process, the method can be used to further study the influence of process parameter variations on the resulting workpiece.

REFERENCES

[1] M. Schlottke-Lakemper, A. Niemöller, M. Meinke, and W. Schröder, "Efficient parallelization for volume-coupled multiphysics simulations on hierarchical cartesian grids," *Computer Methods in Applied Mechanics and Engineering*, vol. 352, pp. 461 – 487, 2019.

[2] M. Geier, M. Schönherr, A. Pasquali, and M. Krafczyk, "The cumulant lattice boltzmann equation in three dimensions: Theory and validation," *Comp. & Math. w. Appl.*, vol. 70, no. 4, pp. 507 – 547, 2015.

[3] M. Milelli, *A numerical analysis of confined turbulent bubble plumes*. PhD thesis, ETH Zurich, 2002.

[4] N. G. Deen, T. Solberg, and B. H. Hjertager, "Large eddy simulation of the gas–liquid flow in a square cross-sectioned bubble column," *Chem. Eng. Sci.*, vol. 56, no. 21, pp. 6341–6349, 2001.

[5] M. Dhotre, N. Deen, B. Niceno, Z. Khan, and J. Joshi, "Large eddy simulation for dispersed bubbly flows: A review," *Int. J. of Chem. Engineering*, vol. 2013, 03 2013.

[6] T. Ma, D. Lucas, T. Ziegenhein, J. Fröhlich, and N. Deen, "Scale-adaptive simulation of a square cross-sectional bubble column," *Chem. Eng. Sci.*, vol. 131, pp. 101–108, 2015.

[7] Z. Liu and B. Li, "Scale-adaptive analysis of euler-euler large eddy simulation for laboratory scale dispersed bubbly flows," *Chem. Eng. Journal*, vol. 338, pp. 465–477, 2018.

[8] M. H. Mohammadi, F. Sotiropoulos, and J. R. Brinkerhoff, "Eulerian-eulerian large eddy simulation of two-phase dilute bubbly flows," *Chem. Eng. Sci.*, vol. 208, p. 115156, 2019.

[9] A. Mühlbauer, M. W. Hlawitschka, and H.-J. Bart, "Models for the numerical simulation of bubble columns: A review," *Chemie Ing. Technik*, vol. 91, no. 12, pp. 1747–1765, 2019.

[10] R. Sungkorn, J. Derksen, and J. Khinast, "Modeling of turbulent gas-liquid bubbly flows using stochastic lagrangian model and lattice-boltzmann scheme," *Chem. Eng. Sci.*, vol. 66, pp. 2745–2757, 06 2011.

[11] S. Shu, N. Yang, F. Bertrand, and J. Chaouki, "High-resolution simulation of oscillating bubble plumes in a square cross-sectioned bubble column with an unsteady k-ε model," *Chem. Eng. Sci.*, 11 2020.

[12] M. Ishii and T. Hibiki, *Thermo-fluid dynamics of two-phase flow*. New York: Springer, second ed., 2011.

[13] A. Sokolichin, G. Eigenberger, and A. Lapin, "Simulation of buoyancy driven bubbly flow: Established simplifications and open questions," *AIChE Journal*, vol. 50, no. 1, pp. 24–45, 2004.

[14] A. Tomiyama, H. Tamai, I. Zun, and S. Hosokawa, "Transverse migration of single bubbles in simple shear flows," *Chem. Eng. Sci.*, vol. 57, no. 11, pp. 1849–1858, 2002.

[15] J. P. Boris, F. F. Grinstein, E. S. Oran, and R. L. Kolbe, "New insights into large eddy simulation," *Fluid Dynamics Research*, vol. 10, pp. 199–228, dec 1992.

[16] A. Lintermann, M. Meinke, and W. Schröder, "Zonal flow solver (ZFS): a highly efficient multi-physics simulation framework," *Int. J. of Comp. Fluid Dynamics*, vol. 34, no. 7-8, pp. 458–485, 2020.

[17] P. L. Bhatnagar, E. P. Gross, and M. Krook, "A model for collision processes in gases. I. small amplitude processes in charged and neutral one-component systems," *Phys. Rev.*, vol. 94, pp. 511–525, May 1954.

[18] Y. H. Qian, D. D'Humières, and P. Lallemand, "Lattice BGK models for navier-stokes equation," *Europhysics Letters (EPL)*, vol. 17, pp. 479–484, feb 1992.

[19] D. Hänel, *Molekulare Gasdynamik: Einführung in die kinetische Theorie der Gase und Lattice-Boltzmann-Methoden*. Berlin Heidelberg: Springer, 2004.

[20] N. G. Deen, B. H. Hjertager, and T. Solberg, "Comparison of piv and lda measurement methods applied to the gas-liquid flow in a bubble column," in *10th Int. Symp. on Appl. of Laser Techniques to Fluid Mech, Lisbon, Portugal, 9-13 July 2000*, 2000.

[21] M. Bouzidi, M. Firdaouss, and P. Lallemand, "Momentum transfer of a boltzmann-lattice fluid with boundaries," *Physics of Fluids*, vol. 13, no. 11, pp. 3452–3459, 2001.

[22] B. Rommes, D. Lauwers, T. Herrig, M. Meinke, W. Schröder, and A. Klink, "Concept for the experimental and numerical study of fluid-structure interaction and gas transport in precise electrochemical machining," in *18th CIRP CMMO, Ljubljana, Slovenia, 15-17 June*, 2021.